

Cite this: *J. Mater. Chem. A*, 2017, 5, 4183

## Self-sacrificed synthesis of carbon-coated SiO<sub>x</sub> nanowires for high capacity lithium ion battery anodes†

Zhaohuai Li,<sup>a</sup> Qiu He,<sup>a</sup> Liang He,<sup>\*a</sup> Ping Hu,<sup>a</sup> Wei Li,<sup>b</sup> Haowu Yan,<sup>a</sup> Xianzhou Peng,<sup>a</sup> Congyun Huang<sup>b</sup> and Liqiang Mai<sup>\*a</sup>

Silicon oxide (SiO<sub>x</sub>) shows great potential for lithium ion battery (LIB) anodes due to its high capacity, environmental friendliness, low cost and high abundance. Herein, we used low-cost mesoporous silica spheres to synthesize core-shell structured porous carbon-coated SiO<sub>x</sub> nanowires (pC-SiO<sub>x</sub> NWs) as a new LIB anode through a novel self-sacrificed method. The one-dimensional structure can accommodate large volume expansion without breaking. The porous carbon coating hinders the penetration of the electrolyte into pC-SiO<sub>x</sub> NWs and formation of a stable solid-electrolyte interphase (SEI) film on the external surface of pC-SiO<sub>x</sub> NWs. As a result, the composite shows excellent cycling stability with high reversible specific capacities of 1060 mA h g<sup>-1</sup> (100 cycles) and 623 mA h g<sup>-1</sup> (150 cycles) at current densities of 100 mA g<sup>-1</sup> and 500 mA g<sup>-1</sup>, respectively. The proposed facile and scalable synthesis is highly competitive for large-scale applications in lithium storage devices/systems.

Received 9th December 2016  
Accepted 21st January 2017

DOI: 10.1039/c6ta10583a

rsc.li/materials-a

### Introduction

Lithium ion batteries (LIBs), which have a high energy density, high capacity and long cycling life, are widely used in our daily life.<sup>1,2</sup> Since the initial commercialization of LIBs two decades ago, LIB anodes have mainly been based on carbonaceous materials.<sup>3</sup> Developing LIB anodes with a higher capacity and more stable cycling performance has been an ongoing challenge. Various LIB anodes with excellent electrochemical performance, such as high capacity, high cycling stability and low cost, have been investigated.<sup>4–8</sup> Graphite and other carbon materials are broadly employed as commercial LIB anodes due to their high conductivity and excellent cycling stability. However, their low theoretical capacity (370 mA h g<sup>-1</sup>) is a limitation for growing pursuit of high capacity energy storage devices.<sup>9,10</sup>

Silicon-based materials are one kind of the most promising LIB anodes due to their high specific capacity. However, the development of silicon-based materials is limited by their huge volumetric and structural variations (their volume shows dramatic expansion even up to 3 or 4 times) during lithiation and delithiation.<sup>11</sup> The volume expansion not only leads to the

cracking and pulverization of silicon-based anodes, but also results in the continuous growth of a solid-electrolyte interphase (SEI) film on the anode surface and rapid capacity fading.<sup>12,13</sup> In order to solve these problems, many researchers are focusing on the synthesis, mechanism and optimization of silicon-based LIB anodes. One promising route is to design and construct nanostructured silicon-based anodes, including nanoparticles,<sup>14,15</sup> ultrathin films,<sup>16–18</sup> nanowires (NWs),<sup>19</sup> core-shell NWs,<sup>20–22</sup> nanopores,<sup>23,24</sup> silicon-based materials@carbon composites or other nanocomposites,<sup>25–28</sup> to accommodate large volume variations. S. Park *et al.* designed a catalyst-free synthesis of Si-SiO<sub>x</sub> core-shell NW anodes.<sup>29</sup> The Si-SiO<sub>x</sub> NW anodes show excellent electrochemical performance, such as a reversible capacity of ~1000 mA h g<sup>-1</sup> even at a high rate of 50C (1C = 3.7 A g<sup>-1</sup>) and a great rate capability. Furthermore, they also reported a low-cost and large-scale approach to prepare interconnected Si/SiO<sub>x</sub> NWs for LIBs.<sup>30</sup> The Si/SiO<sub>x</sub> electrodes show a high reversible capacity of 1280 mA h g<sup>-1</sup> after 150 cycles at a rate of 0.2C, and a high rate capability of ~1200 mA h g<sup>-1</sup> at a 10C rate. These results are based on the fact that silicon acts as an active material and shows a high capacity and superior rate performance. On the other hand, silicon oxide (SiO<sub>x</sub>) with an ultrahigh specific capacity of 1965–2600 mA h g<sup>-1</sup> is much cheaper than silicon, is attracting more and more attention since it can be synthesized from nature's most abundant initial material (silica).<sup>31–36</sup> Liu and co-workers<sup>37</sup> designed and synthesized SiO<sub>x</sub>-C dual-phase glass without Si-C bonds through a sol-gel process followed by pyrolysis, in which a low-cost siloxane (tetraethoxysilane, TEOS) was employed as the precursor. In the synthesized SiO<sub>x</sub>-C dual-phase glass

<sup>a</sup>State Key Laboratory of Advanced Technology for Materials Synthesis and Processing, Wuhan University of Technology, Wuhan 430070, Hubei, P. R. China. E-mail: hel@whut.edu.cn; mlq518@whut.edu.cn

<sup>b</sup>School of Materials Science and Engineering, Wuhan University of Technology, Wuhan 430070, P. R. China

† Electronic supplementary information (ESI) available. See DOI: 10.1039/c6ta10583a

anode, the carbon can alleviate the volume variation of  $\text{SiO}_x$ . Therefore the structural stability and cycling performance of  $\text{SiO}_x$  are significantly enhanced, which delivers a high reversible capacity of  $840 \text{ mA h g}^{-1}$  for 100 cycles at a current density of  $100 \text{ mA g}^{-1}$ . However, the construction of this anode is very complicated and the carbon content of the composite is high, which lead to difficulties in achieving large-scale applications of high-capacity LIBs.

In our work, we paid more attention to one-dimensional  $\text{SiO}_x$ @C nanostructures and designed the core-shell structured porous carbon-coated  $\text{SiO}_x$  NWs (pC- $\text{SiO}_x$  NWs) as a LIB anode. The one-dimensional structure does not pulverize or break into smaller particles after cycling. Furthermore, facile strain relaxation in the NWs allows the increase in their diameter and length without breaking.<sup>19</sup> The flexible carbon coating could alleviate the large mechanical strain during lithiation and delithiation, maintain the integrity of the whole electrode, and meanwhile significantly increase the electrical conductivity.<sup>38,39</sup> The stability of the SEI at the interface between  $\text{SiO}_x$  and the liquid electrolyte is another critical factor in achieving a long cycling life.<sup>40</sup> For a clear comparison of the morphology, structure and performance, we prepared porous silica nanoparticles (p- $\text{SiO}_2$  NPs), porous carbon coated p- $\text{SiO}_2$  NPs (pC-p- $\text{SiO}_2$  NPs), no carbon coated  $\text{SiO}_x$  NWs (nC- $\text{SiO}_x$  NWs) and pC- $\text{SiO}_x$  NWs. Fig. 1 is the schematic of SEI formation on different  $\text{SiO}_x$  nanostructured surfaces, the carbon coating on the exterior surface of  $\text{SiO}_x$  NWs prevents the electrolyte from diffusing into their interior pore space and leads to formation of a stable SEI film,<sup>41,42</sup> which shows that the pC- $\text{SiO}_x$  NWs have a more stable structure during electrochemical cycling. The pC-coating not only increases the electrical conductivity of the anode but also introduces a little carbon into the anode, which increases the specific capacity and the initial coulombic efficiency (ICE) due to lithium trapping in amorphous carbon.<sup>41</sup> However, there are few reports about the synthesis of  $\text{SiO}_x$  NWs in which the initial materials are mainly based on expensive silicon crystals. Most of the synthesis methods are complicated and not fully controllable, including laser ablation,<sup>43</sup> carbon-assisted

growth,<sup>44</sup> chemical vapor deposition (CVD),<sup>45,46</sup> etc. In most cases, the growth mechanism of  $\text{SiO}_x$  NWs is either vapor-liquid-solid (VLS), which requires a nanoscale catalyst as the seed for NWs' growth, or template assisted growth. So the development and application of facile synthesis methods to synthesize  $\text{SiO}_x$  NWs on a large scale and at low cost is highly essential.<sup>47</sup>

## Experimental

All chemicals were purchased from Aladdin or Sigma Aldrich and used as received without further purification.

### Synthesis of bimodal mesoporous silica (BMS) and $\text{SiO}_x$ NWs

1.0 g cetyltrimethylammonium bromide (CTAB) and 1.12 g solid  $\text{Na}_2\text{SiO}_3 \cdot 9\text{H}_2\text{O}$  were dissolved in 17.5 mL deionized (DI) water under vigorous stirring and ultrasonication to form a homogeneous solution. Afterward 1.75 mL ethyl acetate was added into the solution, and then the mixture was maintained at ambient temperature for 5 h followed by water bath treatment at  $90^\circ\text{C}$  for 50 h, and BMS-a was finally obtained. BMS-b can be synthesized from CTAB with an increased amount (up to 1.5 g). After these steps, the BMS was treated with 2 M  $\text{FeCl}_3$  solution, and then dried at  $70^\circ\text{C}$  and roasted at  $400^\circ\text{C}$  for 4 h to get the silica sources. Then put the silica sources in the vapor of ethylenediamine (20 mL ethylenediamine and 10 mL  $\text{H}_2\text{O}$ ) at  $200^\circ\text{C}$  for 30 h, and remove Fe species with 1 M  $\text{HCl}$ . The  $\text{SiO}_x$  NWs were collected by centrifugation and then washed several times with DI water and absolute ethanol.

### Synthesis of pC- $\text{SiO}_x$ NWs

0.1 g  $\text{SiO}_x$  NWs were dispersed in 10 mL DI water, and then mixed with 0.35 g CTAB. After 30 min ultrasonication and 30 min stirring, 0.5 g resorcinol, 45.5 mL absolute ethanol and 0.15 mL  $\text{NH}_3 \cdot \text{H}_2\text{O}$  were added sequentially with stirring for 30 min at  $35^\circ\text{C}$ . Then 0.08 mL formalin was finally added into the mixture and stirred overnight. The core-shell resorcinol-formaldehyde (RF) resin coated  $\text{SiO}_x$  NWs (RF- $\text{SiO}_x$  NWs) were collected by centrifugation and then washed several times with DI water and absolute ethanol. The pC- $\text{SiO}_x$  NWs were prepared by carbonization of the RF- $\text{SiO}_x$  NWs at  $600^\circ\text{C}$  for 5 h in an argon atmosphere.

### Synthesis of p- $\text{SiO}_2$ NPs and pC-p- $\text{SiO}_2$ NPs

The p- $\text{SiO}_2$  NPs were prepared according to a modified Stober method.<sup>48</sup> In brief, 0.1 g CTAB, 46 mL ethanol and 2.5 mL tetraethyl orthosilicate (TEOS) were mixed in a beaker under vigorous stirring, followed by injection of 5 mL 28% ammonia solution and stirring for 4 h. The  $\text{SiO}_2$  NPs were collected by centrifugation and then washed several times with DI water and absolute ethanol. The pC-p- $\text{SiO}_2$  NPs were synthesized under the same treatment conditions as those of pC- $\text{SiO}_x$  NWs.

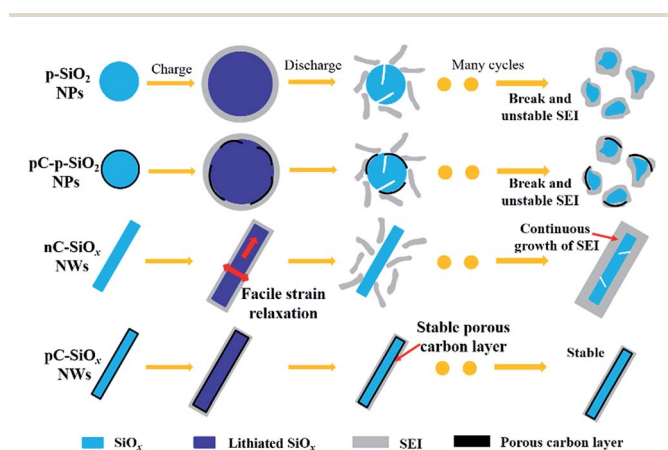


Fig. 1 Schematic illustration of different  $\text{SiO}_x$  nanostructures before and after charge-discharge cycling, indicating that pC- $\text{SiO}_x$  NWs have a more stable structure during electrochemical cycling.

## Characterization

X-ray diffraction (XRD) characterization was performed to investigate the crystallographic information of samples using a D8 Advance X-ray diffractometer with a non-monochromated Cu K $\alpha$  X-ray source ( $\lambda = 1.054056 \text{ \AA}$ ). Scanning electron microscopy (SEM) images were collected by using a JEOL JSM-7100F at an acceleration voltage of 15 kV. Transmission electron microscopy (TEM) and high resolution TEM (HRTEM) images were recorded with a JEM-2100F microscope. Brunauer–Emmett–Teller (BET) surface areas were measured using a Tristar II 3020 instrument by nitrogen adsorption at 77 K. Thermogravimetric analysis (TGA) was performed using a Netzsch STA 449C simultaneous analyzer. Raman spectra were obtained using a Renishaw inVia micro-Raman spectroscopy system. X-ray photoelectron spectroscopy (XPS) measurements were conducted using a VG MultiLab 2000 instrument.

## Electrochemical characterization

CR 2016 coin cells were assembled in a glovebox filled with pure argon gas. Lithium foil was used as the counter electrode, and a solution of LiPF $_6$  (1 M) in ethylene carbonate/diethyl carbonate (1 : 1 v/v) was used as the electrolyte. The working electrode was made of active materials (80 wt%), carbon black (10 wt%) and PVDF (10 wt%) in *N*-methyl pyrrolidone (NMP) by stirring for 1 h. Then, the slurry was coated on Cu foil and dried overnight at 70 °C to obtain the working electrode. The battery was aged for 12 h before testing to ensure full absorption of the electrolyte into the electrodes. The mass loading of the active material was 1.0–1.2 mg cm $^{-2}$ . Galvanostatic charge/discharge measurements were performed with a multichannel battery testing system (LAND CT2001A) in the potential range from 0.01 to 3.0 V at different current densities. Electrochemical impedance spectroscopy (EIS) tests were conducted on an electrochemical workstation (Autolab PGSTAT302N).

## Results and discussion

Low-cost BMS<sup>49–51</sup> was used as the precursor for the synthesis of SiO $_x$  NWs. Fig. 2 shows the schematic illustration of the time-dependent solvothermal reaction process and corresponding SEM images of samples at different stages. The iron-assisted method is applied to prepare SiO $_x$  NWs in the vapor of ethylenediamine. Ethylenediamine is utilized as the solvent and

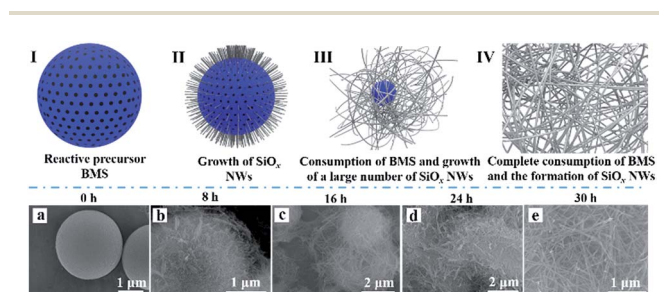


Fig. 2 Schematic illustration of the time-dependent solvothermal reaction (from BMS to SiO $_x$  NWs): self-sacrificed evolution mechanism.

slowly etches the precursor of BMS, Fe $^{3+}$  is loaded in the pores of BMS and acts as the catalyst. After being treated in amine vapor for 8 h, the SiO $_x$  NWs are grown on the surfaces of BMS spheres along the direction of the (001) crystal plane with the lowest energy under the help of iron (Fig. 2II). Then, as the reaction is carried out, the ethylenediamine steam consumes the BMS slowly, and the NWs gradually grow from BMS spheres by consuming the silica nutrition in BMS (Fig. 2III) simultaneously. Finally, when the reaction is completed (30 h), all the BMS will be completely sacrificed and the pure SiO $_x$  NWs are obtained (Fig. 2IV).

Fig. 3a–d present the SEM, TEM and HRTEM images of SiO $_x$  NWs. The as-synthesized SiO $_x$  NWs with diameters of 20–50 nm have a smooth surface and their lengths are several micrometers. The corresponding HRTEM image indicates the lattice fringes of SiO $_x$  NWs with a *d*-spacing of  $\sim 4.83 \text{ \AA}$ . The energy dispersive spectrometry (EDS) spectra of nC–SiO $_x$  NWs and pC–SiO $_x$  NWs were collected from the regions marked by the white rectangle frame in Fig. 3e and f, respectively. Fig. 3g shows that the atomic ratio of Si : O is approximately 1 : 1.65, which demonstrates that the as-synthesized SiO $_x$  NWs and pC–SiO $_x$  NWs have oxygen vacancies. These results imply that the atomic ratio of Si : O will not change after calcination in argon at 600 °C. Fig. S1† shows the SEM images of two kinds of BMS precursors with different specific surface areas and their nitrogen adsorption measurement results. The BMS with low and high specific surface areas are denoted as BMS-a (which is used to synthesize SiO $_x$  NWs) and BMS-b, respectively. From the SEM images of BMS, monodisperse BMS with a large number of mesopores on its surface can be clearly observed (Fig. S1, the inset of a and b†). According to the BET calculation, the specific surface areas of BMS-a and BMS-b are 501 and 710 m $^2 \text{ g}^{-1}$ , respectively (Fig. S1c†), which provide abundant reactive sites during the growth of SiO $_x$  NWs. The pore size is mainly distributed in a range of 5–10 nm (Fig. S1d†). It is interesting

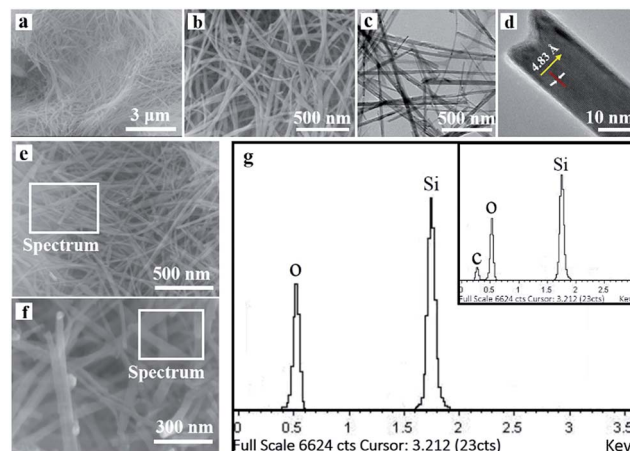


Fig. 3 Characterization of SiO $_x$  NWs. SEM (a, b), TEM (c) and HRTEM (d) images of SiO $_x$  NWs. The SEM images of SiO $_x$  NWs (e) and pC–SiO $_x$  NWs (f). The EDS spectra (g) collected from the regions marked by the white rectangle frame in the SEM images (e, f), showing that the atomic ratio of Si : O is 1 : 1.65.

that shorter  $\text{SiO}_x$  NWs ( $\text{SiO}_x$  NWs-b) are obtained under the same synthetic conditions when BMS-b is employed as the precursor. The SEM, TEM and HRTEM images of  $\text{SiO}_x$  NWs-b are shown in Fig. S2(a-d).<sup>†</sup> The XRD patterns of the BMS,  $\text{SiO}_x$  NWs and  $\text{SiO}_x$  NWs-b are shown in Fig. S3,<sup>†</sup> indicating the crystallinity of  $\text{SiO}_x$  NWs and  $\text{SiO}_x$  NWs-b, which is consistent with the above HRTEM image (Fig. 3d) and previous report.<sup>47</sup>

To further determine the value of  $x$  in the  $\text{SiO}_x$  NWs, the concentration of oxygen vacancies of  $\text{SiO}_x$  NWs was characterized using TGA. TGA of  $\text{SiO}_x$  NWs (Fig. S4a<sup>†</sup>) indicates that the  $\text{SiO}_x$  NWs react with oxygen during heating in air, leading to mass increase compared with the  $\text{SiO}_x$  annealed in argon. The EDS of the  $\text{SiO}_x$  NWs (Fig. S4b<sup>†</sup>) after annealing in air at 800 °C shows that the atomic ratio of Si : O is 1 : 1.98. The concentration of oxygen vacancies is calculated from the difference in weight increase between the two TGA curves. From the calculation, we estimate that the  $x$  value in  $\text{SiO}_x$  NWs is 1.66; the result is consistent with the EDS test result.

Subsequently, the obtained  $\text{SiO}_x$  NWs were successively coated with RF resin by a solution method and no SiC was formed on the surface of the  $\text{SiO}_x$  NWs, which is electrochemically inert to lithium.<sup>52</sup> The schematic diagram of the RF-coating is shown in Fig. 4I–III. First of all, polymer precursor RF coated  $\text{SiO}_x$  NWs (RF- $\text{SiO}_x$  NWs) were obtained by a suspension method (Fig. 4II), and then the intermediate product was carbonized in an argon atmosphere at 600 °C to obtain pC- $\text{SiO}_x$  NWs (Fig. 4III). Fig. 4a shows that the  $\text{SiO}_x$  NWs are completely coated by RF resin. Representative TEM images of pC- $\text{SiO}_x$  NWs are shown in Fig. 4b, indicating the carbon coating with the thickness of around 2 nm. Fig. 4c shows that the NW structure is preserved well after carbonization in an argon atmosphere at 600 °C, and the corresponding EDS elemental mappings indicate that Si, O and C are homogeneously distributed in pC- $\text{SiO}_x$  NWs (Fig. 4d–f). It is worth mentioning that the  $\text{SiO}_x$  NWs were fractured to be shorter because of vigorous string during the synthesis process of RF-

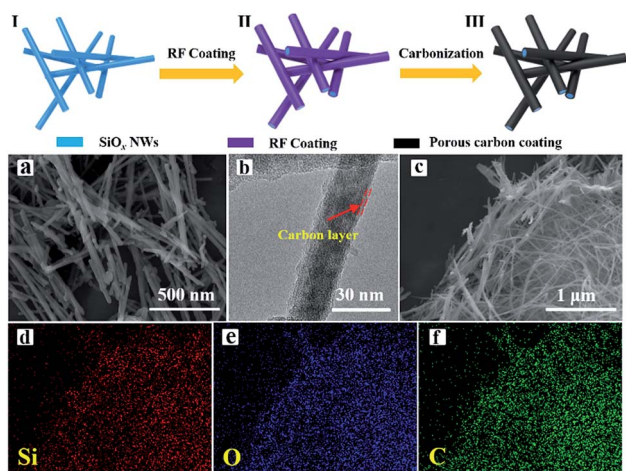


Fig. 4 Characterization of pC- $\text{SiO}_x$  NWs. Schematic of pC- $\text{SiO}_x$  NWs' formation (I–III), SEM image of RF- $\text{SiO}_x$  NWs (a) and TEM image of pC- $\text{SiO}_x$  NWs (b). The SEM image of pC- $\text{SiO}_x$  NWs (c) and corresponding EDS elemental mappings (d–f).

$\text{SiO}_x$  NWs (Fig. S5<sup>†</sup>). The aforementioned synthesis approach has the following three advantages. First, the cost of chemicals used in the synthesis ( $\text{Na}_2\text{SiO}_3 \cdot 9\text{H}_2\text{O}$ , CTAB, ethyl acetate, ethylenediamine resorcinol, formaldehyde and ammonia) is low, providing high possibility and potential for large-scale production. Second, synthesis conditions (gas–solid hydrothermal process and carbonization) are facile and controllable. Third,  $\text{SiO}_x$  NWs can be thoroughly coated by RF resin, so the core–shell structure is easily obtained.

Fig. 5a provides XPS results that confirm the existence of  $\text{SiO}_x$  and carbon. Compared with carbon, the negligible signal of Si and O in the XPS spectrum (inset image) shows a very low atomic percentage of  $\text{SiO}_x$  around the sample's surface, clearly indicating that the carbon coating fully wraps the  $\text{SiO}_x$  NWs, which is consistent with the SEM and TEM images (Fig. 4a and b). Notably, the high-resolution C 1s core level XPS spectrum (Fig. S6<sup>†</sup>) can be deconvoluted into three components:  $\text{sp}^2$  bonded C at 284.6 eV (70.12%), C in the C–O bond at 285.9 eV (17.56%), and C in the C=O bond at 288.4 eV (12.32%).<sup>53</sup> It shows that there is no C–Si bond existed in pC- $\text{SiO}_x$  NWs, indicating that the SiC inert material was not generated during the preparation of pC- $\text{SiO}_x$  NWs. The mass percentage of  $\text{SiO}_x$  in pC- $\text{SiO}_x$  NWs is found to be ~90.67% by TGA as shown in Fig. 5b. The carbon content in the synthesized core–shell pC- $\text{SiO}_x$  NWs is less than that of previous report,<sup>35</sup> which could pose positive effects on the capacity of the anodes.

As shown in Fig. 6, the nature of carbon in pC- $\text{SiO}_x$  NWs was confirmed by Raman characterization. Two broad peaks located at 1363 and 1594  $\text{cm}^{-1}$  are assigned to the D and G bands of carbon, respectively.<sup>54</sup> The Raman spectrum of pC- $\text{SiO}_x$  NWs also displays the amorphous feature of the carbon shell.<sup>55</sup>

Fig. 7 shows the electrochemical performance of the above four nanostructured anodes. As shown in Fig. S7a,<sup>†</sup> the p- $\text{SiO}_2$  NPs have a diameter of ~100 nm. The BET curves (Fig. S7b<sup>†</sup>) show that the specific surface area of p- $\text{SiO}_2$  NPs is 59.24  $\text{m}^2 \text{g}^{-1}$ , and the pore size is mainly distributed in a range of 5–10 nm. The SEM image of pC-p- $\text{SiO}_2$  NPs is shown in Fig. S7c,<sup>†</sup> and the TGA shows that the mass percentage of  $\text{SiO}_2$  in pC-p- $\text{SiO}_2$  NPs (~90.44%) is close to that of pC- $\text{SiO}_x$  NWs. The cycling performances of the above electrodes were evaluated using charge/discharge galvanostatic cycling from 0.01 to 3.0 V, and all of

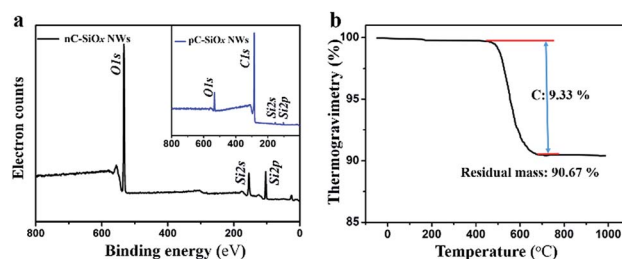


Fig. 5 (a) XPS spectra of nC- $\text{SiO}_x$  NWs and pC- $\text{SiO}_x$  NWs (inset). Inset image shows that the signals of Si and O are significantly low compared with that of carbon, indicating that  $\text{SiO}_x$  NWs are completely covered by carbon. (b) TGA profile of pC- $\text{SiO}_x$  NWs. The TGA curve demonstrates that the pC- $\text{SiO}_x$  NWs contain a little carbon.

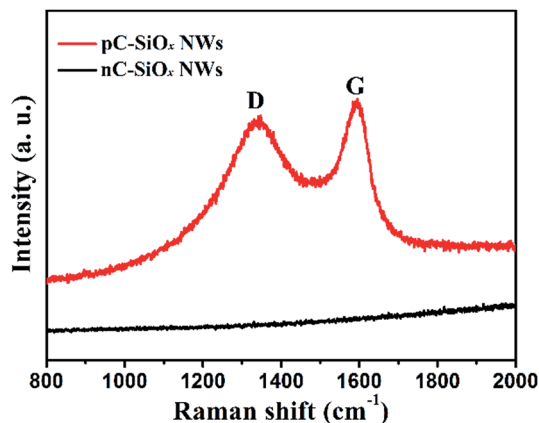


Fig. 6 Raman spectra of pC-SiO<sub>x</sub> NWs and nC-SiO<sub>x</sub> NWs.

the capacities are calculated based on the total mass of the active materials (SiO<sub>x</sub> and C in the pC-SiO<sub>x</sub> NWs). The cycling curves (Fig. 7a) of the assembled cells based on p-SiO<sub>2</sub> NPs, pC-p-SiO<sub>2</sub> NPs, nC-SiO<sub>x</sub> NWs and pC-SiO<sub>x</sub> NWs show that the pC-SiO<sub>x</sub> NWs deliver a higher capacity than p-SiO<sub>2</sub> NPs, pC-p-SiO<sub>2</sub> NPs and nC-SiO<sub>x</sub> NWs at a current density of 100 mA g<sup>-1</sup>. The p-SiO<sub>2</sub> NPs show a low capacity of ~230 mA h g<sup>-1</sup> over 100 cycles and a first discharge capacity of only 733 mA h g<sup>-1</sup>, in addition, the ICE of the p-SiO<sub>2</sub> NPs anode is 33%. The pC-p-SiO<sub>2</sub> NPs also display an unsatisfactory capacity at the current density of 100 mA g<sup>-1</sup>. The poor electrochemical performance of the p-SiO<sub>2</sub> NPs and pC-p-SiO<sub>2</sub> NPs is attributed to their large volume expansion, which makes the anode collapse and lose contact with the current collector, and the quick attenuation of their specific capacity. Furthermore, the electrode pulverization also leads to the collapse of the SEI layer on the anode surface. Consequently, lithium ions will react with active materials associated with consuming a large number of lithium ions to form a sustainable SEI film. The nC-SiO<sub>x</sub> NWs' unique one-dimensional nanostructure can buffer the volume expansion during the insertion and extraction of lithium. The first discharge capacity significantly increases to 1315 mA h g<sup>-1</sup> and the capacity reaches a stable level at 473 mA h g<sup>-1</sup> over 100 cycles, showing an increasing trend. However, the specific capacity is not high enough as we expected. In contrast, the electrochemical performance of SiO<sub>x</sub> NWs can be optimized by pC-coating on their surfaces. The constructed pC-SiO<sub>x</sub> NWs deliver a high initial discharge capacity (2215 mA h g<sup>-1</sup>) and high stability during repeated electrochemical lithiation/delithiation cycles. A high capacity (~1060 mA h g<sup>-1</sup>) is retained after 100 cycles. The pC-coating by pyrolysis has a relatively low Young's modulus and hardness compared with SiO<sub>x</sub>,<sup>56,57</sup> which is more suitable for applications with large elastic deformation and could avoid the capacity loss of pC-SiO<sub>x</sub> NW anodes. EIS characterization was carried out after the completion of the first cycle at the fully delithiated state (held at 2.5 V vs. Li<sup>+</sup>/Li) (Fig. 7b), and it is obvious that the electrical conductivity can be significantly improved by carbon coating. The electrical conductivity of pC-SiO<sub>x</sub> NWs is much higher than that of other three kinds of structures. However, EIS curves also

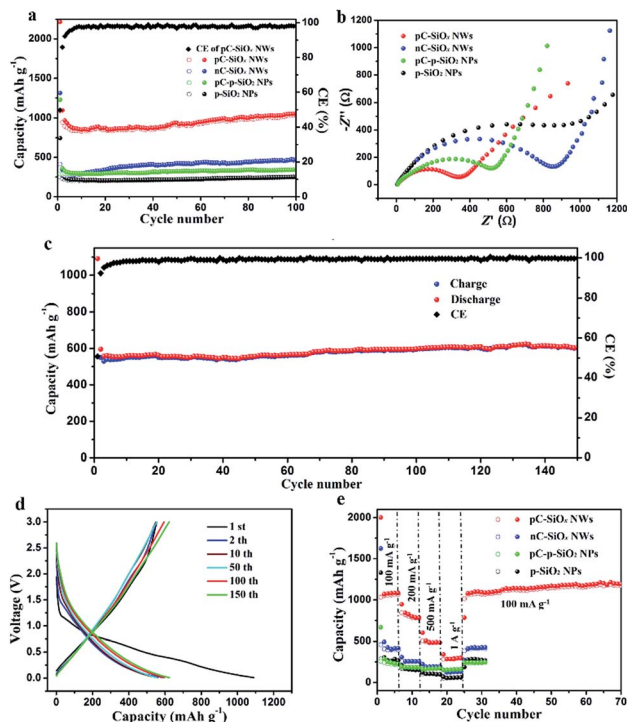


Fig. 7 Electrochemical characterizations. All the specific capacities of the anodes are based on the total mass of the active materials (SiO<sub>x</sub> and C in pC-SiO<sub>x</sub> NWs). (a) The cycling performance of pC-SiO<sub>x</sub> NWs, nC-SiO<sub>x</sub> NWs, pC-p-SiO<sub>2</sub> NPs and p-SiO<sub>2</sub> NPs. The mass loading of active materials is around 1.0 mg cm<sup>-2</sup>, and the current density is 100 mA g<sup>-1</sup>. (b) Nyquist plots of pC-SiO<sub>x</sub> NWs, nC-SiO<sub>x</sub> NWs, pC-p-SiO<sub>2</sub> NPs and p-SiO<sub>2</sub> NPs after the completion of the first delithiation. (c) The cycling performance of pC-SiO<sub>x</sub> NWs at a current density of 500 mA g<sup>-1</sup>. (d) Voltage profiles of pC-SiO<sub>x</sub> NWs plotted for the first, 2nd, 10th, 50th, 100th, and 150th cycles at a current density of 500 mA g<sup>-1</sup>. (e) Rate capability of pC-SiO<sub>x</sub> NWs, nC-SiO<sub>x</sub> NWs, pC-p-SiO<sub>2</sub> NPs and p-SiO<sub>2</sub> NPs at various current densities.

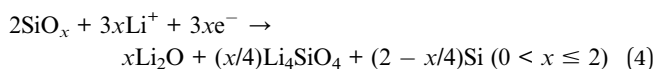
imply the inferior electron diffusion ability which is due to the fact that the carbon coating limits the lithium ions' embedding rate.

The pC-SiO<sub>x</sub> NWs also display a satisfactory performance at a larger current density. The discharge capacity of the pC-SiO<sub>x</sub> NWs anode remains around 623 mA h g<sup>-1</sup> after 150 cycles at 500 mA g<sup>-1</sup> (Fig. 7c). The voltage profiles of pC-SiO<sub>x</sub> NWs are shown in Fig. 7d. The shape of the profiles does not change from the 2<sup>nd</sup> to the 150<sup>th</sup> cycle, indicating a stable electrochemical behavior of the pC-SiO<sub>x</sub> NWs anode, showing more evidence of their advantages in electrochemical applications. The morphologies of SiO<sub>x</sub> NWs after 150 electrochemical cycles at the current density of 500 mA g<sup>-1</sup> are shown in Fig. S8,<sup>†</sup> which further verify the structural stability of SiO<sub>x</sub> NWs. It is clear that the diameter of pC-SiO<sub>x</sub> NWs is increased and the surface becomes rough due to the volume expansion and the SEI formation. However, the NW structure is still preserved well without obvious fractures, associating with good cycling stability. Although they have a low ICE resulting from the volume expansion, an irreversible SEI and the formation of Li<sub>4</sub>SiO<sub>4</sub> and Li<sub>2</sub>O, the CE values of following cycles are

maintained at more than 99%. The chemical equations of electrochemical lithiation of silicon oxide are expressed as follows.<sup>37</sup>



According to eqn (1)–(3), eqn (4) can be obtained as follows.



The reaction of silicon and lithium ions would generate a lithium–silicon alloy, which contributes to the capacity of LIBs.



As shown in eqn (4), we know that the electrochemically inert products  $\text{Li}_2\text{O}$  and  $\text{Li}_4\text{SiO}_4$  are generated and lead to a large irreversible capacity in the first charge–discharge cycle.  $\text{SiO}_x$  NWs with a smaller  $x$  value will lead to the generation of less  $\text{Li}_2\text{O}$  and  $\text{Li}_4\text{SiO}_4$ , which is an effective way to improve the ICE. However, in our synthesis, the  $x$  is nearly a constant value. So, it is an ongoing challenge for us to improve the ICE of  $\text{SiO}_x$  anode. Fortunately,  $\text{Li}_2\text{O}$  and  $\text{Li}_4\text{SiO}_4$  can act as the buffer to alleviate volume expansion of the  $\text{SiO}_x$  anode and effectively prevent the active silicon from aggregation, and silicon can fully react with lithium ions (eqn (5)). The increased capacity should be caused by the following two reasons: (1) the slow velocity of lithium ions that enter into the  $\text{SiO}_x$  NWs' core and (2) slow generation of active silicon with the increase of cycle numbers (eqn (4)).<sup>58</sup>

Their rate capabilities were further investigated at various current densities ranging from 0.1 to 1 A  $\text{g}^{-1}$  (Fig. 7e). The p- $\text{SiO}_2$  NPs, the pC-p- $\text{SiO}_2$  NPs and the nC- $\text{SiO}_x$  NWs show comparably low capacities at high current densities (0.5 to 1 A  $\text{g}^{-1}$ ). These results indicate that the nC- $\text{SiO}_x$  NWs cannot thoroughly sustain drastic volume variation which is associated with the formation of an unstable SEI film at large current densities. Furthermore, nC- $\text{SiO}_x$  NWs' low electrical conductivity would pose other negative effects. In contrast, the pC- $\text{SiO}_x$  NWs show the most remarkable rate capability. The assembled cell was first cycled at 100 mA  $\text{g}^{-1}$  for 6 cycles, followed by cycling with a stepwise increase of charge/discharge rates to as high as 1 A  $\text{g}^{-1}$ . The pC- $\text{SiO}_x$  NWs show high initial reversible discharge and charge capacities of 2001 and 1032 mA h  $\text{g}^{-1}$  at the current density of 100 mA  $\text{g}^{-1}$  respectively. An average reversible capacity of  $\sim 511$  mA h  $\text{g}^{-1}$  ( $\sim 309$  mA h  $\text{g}^{-1}$ ) is obtained at 500 mA  $\text{g}^{-1}$  (1 A  $\text{g}^{-1}$ ). The capacity of 500 mA  $\text{g}^{-1}$  is not fully consistent with Fig. 6c due to the fact that the capacity increases slowly, which is attributed to the gradually produced silicon. When the rate is directly reduced to 100 mA  $\text{g}^{-1}$  again, the capacity increases to  $\sim 1170$  mA h  $\text{g}^{-1}$  and remains stable for the following cycles. The stable trend is in good agreement with its cycling stability.

## Conclusions

In summary, we demonstrate an effective design and construction of a low-cost  $\text{SiO}_x$  NWs LIB anode with a stable cycling life and high specific capacity. The  $\text{SiO}_x$  NWs are synthesized by a self-sacrificed method in the vapor of ethylenediamine combined with a facile iron-assisted route. The core–shell pC- $\text{SiO}_x$  NWs with a high structural integrity could prevent continuous formation of the SEI. The pC- $\text{SiO}_x$  NWs anode maintains the capacity around 1060 mA h  $\text{g}^{-1}$  at a rate of 100 mA  $\text{g}^{-1}$  after 100 cycles, or 623 mA h  $\text{g}^{-1}$  at a rate of 500 mA  $\text{g}^{-1}$  after 150 cycles. The proposed synthesis and construction process is facile, scalable, highly reproducible, and compatible with slurry coating manufacturing technology. The synthesized pC- $\text{SiO}_x$  NWs are promising candidates for LIB anodes in which the fracture of anodes and stability of the SEI are two critical problems. By combining economic synthesis of NWs with prelithiation techniques, the scalable, industrially compatible and generally applicable approach will open up a promising opportunity for the forthcoming low-cost and high-capacity batteries.

## Acknowledgements

This work was supported by the National Key Research and Development Program of China (2016YFA0202603 and 2016YFA0202604), the National Basic Research Program of China (2013CB934103), the National Natural Science Foundation of China (51521001, 51502227, and 51579198), the China Postdoctoral Science Foundation (2015T80845), the Hubei Province Natural Science Fund (2016CFB582), and the Fundamental Research Funds for the Central Universities (WUT: 2016III001 and 2016III005).

## Notes and references

- 1 J. M. Tarascon and M. Armand, *Nature*, 2001, **414**, 359–367.
- 2 K. T. Nam, D. W. Kim, P. J. Yoo, C. Y. Chiang, N. Meethong, P. T. Hammond, Y. M. Chiang and A. M. Belcher, *Science*, 2006, **312**, 885–888.
- 3 M. Armand and J. M. Tarascon, *Nature*, 2008, **451**, 652–657.
- 4 H. Liu, S. Chen, G. X. Wang and S. Z. Qiao, *Chem.-Eur. J.*, 2013, **19**, 16897–16901.
- 5 Y. Wang, L. Yu and X. W. Lou, *Angew. Chem., Int. Ed.*, 2016, **128**, 14888–14892.
- 6 W. Ren, Z. Zheng, Y. Luo, W. Chen, C. Niu, K. Zhao, M. Yan, L. Zhang, J. Meng and L. Mai, *J. Mater. Chem. A*, 2015, **3**, 19850–19856.
- 7 K. Zhao, L. Zhang, R. Xia, Y. Dong, W. Xu, C. Niu, L. He, M. Yan, L. Qu and L. Mai, *Small*, 2016, **12**, 588–594.
- 8 L. Xia, S. Wang, G. X. Liu, L. X. Ding, D. D. Li, H. H. Wang and S. Z. Qiao, *Small*, 2016, **12**, 853–859.
- 9 W. J. Zhang, *J. Power Sources*, 2011, **196**, 877–885.
- 10 J. R. Dahn, T. Zheng, Y. Liu and J. S. Xue, *Science*, 1995, **270**, 590–593.
- 11 X. H. Liu, J. W. Wang, S. Huang, F. Fan, X. Huang, Y. Liu, S. Krylyuk, J. Yoo, S. A. Dayeh, A. V. Davydov, S. X. Mao,

- S. T. Picraux, S. Zhang, J. Li, T. Zhu and J. Y. Huang, *Nat. Nanotechnol.*, 2012, 7, 749–756.
- 12 H. Wu and Y. Cui, *Nano Today*, 2012, 7, 414–429.
- 13 N. Liu, Z. Lu, J. Zhao, M. T. McDowell, H. W. Lee, W. Zhao and Y. Cui, *Nat. Nanotechnol.*, 2014, 9, 187–192.
- 14 Y. Yao, J. Zhang, L. Xue, T. Huang and A. Yu, *J. Power Sources*, 2011, 196, 10240–10243.
- 15 H. Wu, G. Yu, L. Pan, N. Liu, M. T. McDowell, Z. Bao and Y. Cui, *Nat. Commun.*, 2013, 4, 131–140.
- 16 B. Gao, S. Sinha, L. Fleming and O. Zhou, *Adv. Mater.*, 2001, 13, 816–819.
- 17 T. Takamura, S. Ohara, M. Uehara, J. Suzuki and K. Sekine, *J. Power Sources*, 2004, 129, 96–100.
- 18 H. Kim, B. Han, J. Choo and J. Cho, *Angew. Chem.*, 2008, 120, 10305–10308.
- 19 C. K. Chan, H. Peng, G. Liu, K. Mcilwrath, X. F. Zhang, R. A. Huggins and Y. Cui, *Nat. Nanotechnol.*, 2008, 3, 31–35.
- 20 J. S. Lee, S. T. Kim, R. Cao, N. S. Choi, M. Liu, K. T. Lee and J. Cho, *Adv. Energy Mater.*, 2011, 1, 34–50.
- 21 T. H. Hwang, Y. M. Lee, B. S. Kong, J. S. Seo and J. W. Choi, *Nano Lett.*, 2012, 12, 802–807.
- 22 T. D. Bogart, D. Oka, X. Lu, M. Gu, C. Wang and B. A. Korgel, *ACS Nano*, 2014, 8, 915–922.
- 23 X. Cao, X. Chuan, R. C. Massé, D. Huang, S. Li and G. Cao, *J. Mater. Chem. A*, 2015, 3, 22739–22749.
- 24 D. Perez-Fernandez, D. Shcherbakov, T. Matt, N. C. Leong, I. Kudyba, S. Duscha, H. Boukari, R. Patak, S. R. Dubbaka, K. Lang, M. Meyer, R. Akbergenov, P. Freihofer, S. Vaddi, P. Thommes, V. Ramakrishnan, A. Vasella and E. C. Böttger, *Nat. Commun.*, 2014, 5, 3112.
- 25 J. Ji, H. Ji, L. L. Zhang, X. Zhao, X. Bai, X. Fan, F. Zhang and R. S. Ruoff, *Adv. Mater.*, 2013, 25, 4673–4677.
- 26 D. S. Jung, T. H. Hwang, S. B. Park and J. W. Choi, *Nano Lett.*, 2013, 13, 2092–2097.
- 27 Y. Ren and M. Li, *J. Power Sources*, 2016, 306, 459–466.
- 28 L. Zhang, J. Deng, L. Liu, W. Si, S. Oswald, L. Xi, M. Kundu, G. Ma, T. Gemming, S. Baunack, F. Meyer, C. Yan and O. G. Schmidt, *Adv. Mater.*, 2014, 26, 4527–4532.
- 29 K. W. Lim, J. I. Lee, J. Yang, Y. K. Kim, H. Y. Jeong, S. Park and H. S. Shin, *ACS Appl. Mater. Interfaces*, 2014, 6, 6340–6345.
- 30 S. Yoo, J. I. Lee, M. Shin and S. Park, *ChemSusChem*, 2013, 6, 1153–1157.
- 31 W. Wu, J. Shi, Y. Liang, F. Liu, Y. Peng and H. Yang, *Phys. Chem. Chem. Phys.*, 2015, 17, 13451–13456.
- 32 M. Li, Y. Zeng, Y. Ren, C. Zeng, J. Gu, X. Feng and H. He, *J. Power Sources*, 2015, 288, 53–61.
- 33 J. Tu, Y. Yuan, P. Zhan, H. Jiao, X. Wang, H. Zhu and S. Jiao, *J. Phys. Chem. C*, 2014, 118, 7357–7362.
- 34 Y. Zhang, Y. Li, Z. Wang and K. Zhao, *Nano Lett.*, 2014, 14, 7161–7170.
- 35 Y. Liang, L. Cai, L. Chen, X. Lin, R. Fu, M. Zhang and D. Wu, *Nanoscale*, 2015, 7, 3971–3975.
- 36 J. Zhao, H. W. Lee, J. Sun, K. Yan, Y. Liu, W. Liu, Z. Lu, D. Lin, G. Zhou and Y. Cui, *Proc. Natl. Acad. Sci.*, 2016, 113, 7408–7413.
- 37 P. Lv, H. Zhao, C. Gao, Z. Du, J. Wang and X. Liu, *J. Power Sources*, 2015, 274, 542–550.
- 38 C. Niu, M. Huang, P. Wang, J. Meng, X. Liu, X. Wang, K. Zhao, Y. Yu, Y. Wu, C. Lin and L. Mai, *Nano Res.*, 2016, 9, 128–138.
- 39 J. Liang, X. Y. Yu, H. Zhou, H. B. Wu, S. Ding and X. W. Lou, *Angew. Chem., Int. Ed.*, 2014, 53, 12803–12807.
- 40 H. Wu, G. Chan, J. W. Choi, I. Ryu, Y. Yao, M. T. McDowell, S. W. Lee, A. Jackson, Y. Yang, L. Hu and Y. Cui, *Nat. Nanotechnol.*, 2012, 7, 310–315.
- 41 Z. Lu, N. Liu, H. W. Lee, J. Zhao, W. Li, Y. Li and Y. Cui, *ACS Nano*, 2015, 9, 2540–2547.
- 42 R. Huang, X. Fan, W. Shen and J. Zhu, *Appl. Phys. Lett.*, 2009, 95, 133119.
- 43 J. C. Wang, C. Z. Zhan and F. G. Li, *Solid State Commun.*, 2003, 125, 629–631.
- 44 K. H. Lee, H. S. Yang, K. H. Baik, J. Bang, R. R. Vanfleet and W. Sigmund, *Chem. Phys. Lett.*, 2004, 383, 380–384.
- 45 S. H. Li, X. F. Zhu and Y. P. Zhao, *J. Phys. Chem. B*, 2004, 108, 17032–17041.
- 46 J. Hu, Y. Jiang, X. Meng, C. S. Lee and S. T. Lee, *Small*, 2005, 1, 429–438.
- 47 P. Chen, S. Xie, N. Ren, Y. Zhang, A. Dong, Y. Chen and Y. Tang, *J. Am. Chem. Soc.*, 2006, 128, 1470–1471.
- 48 W. Stöber, A. Fink and E. Bohn, *J. Colloid Interface Sci.*, 1968, 26, 62–69.
- 49 G. Schulz-Ekloff, J. Rathouský and A. Zukal, *Int. J. Inorg. Mater.*, 1999, 1, 97–102.
- 50 F. Zhang, Y. Yan, Y. Meng, Y. Xia, B. Tu and D. Zhao, *Microporous Mesoporous Mater.*, 2007, 98, 6–15.
- 51 X. Wang, W. Li, G. Zhu, S. Qiu, D. Zhao and B. Zhong, *Microporous Mesoporous Mater.*, 2004, 71, 87–97.
- 52 C. K. Chan, R. N. Patel, M. J. O'Connell, B. A. Korgel and Y. Cui, *ACS Nano*, 2010, 4, 1443–1450.
- 53 X. Li, Y. Liu, X. Song, H. Wang, H. Gu and H. Zeng, *Angew. Chem., Int. Ed.*, 2015, 54, 1759–1764.
- 54 L. Sun, L. Wang, C. Tian, T. Tan, Y. Xie, K. Shi, M. Li and H. Fu, *RSC Adv.*, 2012, 2, 4498–4506.
- 55 Q. Tian, Y. Tian, Z. Zhang, L. Yang and S. I. Hirano, *J. Power Sources*, 2014, 269, 479–485.
- 56 P. Zhou, X. Yang, L. He, Z. Hao, W. Luo, B. Xiong, X. Xu, C. Niu, M. Yan and L. Mai, *Appl. Phys. Lett.*, 2015, 106, 111908.
- 57 L. He, M. Toda, Y. Kawai, H. Miyashita, M. Omori, T. Hashida, R. Berger and T. Ono, *Microsyst. Technol.*, 2014, 20, 201–208.
- 58 X. Luo, H. Zhang, W. Pan, J. Gong, B. Khalid, M. Zhong and H. Wu, *Small*, 2015, 11, 6009–6012.